PCCP

PAPER

View Article Online
View Journal

Cite this: DOI: 10.1039/d5cp04727g

Photoinduced electron transfer (PET) in ethaline-like solvents

Saqib Rabbani,[a] Mohammedulameen Fakhri,[a] Andy Lin,[a] Sasha Noble[ab] and John R. Swierk *[a]

Received 5th December 2025,
Accepted 7th April 2026

DOI: 10.1039/d5cp04727g

rsc.li/pccp

Deep eutectic solvents (DESs) are 21st century solvents composed entirely of hydrogen bond donors and acceptors, which form a eutectic solvent having a significantly lower melting point than its individual components. Due to their tunable nature, DESs are widely employed for applications in electrochemistry, nanotechnology, catalysis and synthesis but their intrinsic electron transfer behaviour is largely unexplored. In order to characterize electron transfer in DESs, steady state reductive emission quenching measurements were performed using tris(2,2′-bipyridine)ruthenium(II), $[Ru(bpy)_3]^{2+}$, with a series of quenchers in several different volumetric compositions of ethaline (choline chloride:ethylene glycol) and water. Using Stern–Volmer analysis, rate constant (k_q) values for excited state quenching were calculated and compared with diffusion limited rate constant (k_D) data. Finally, the electron transfer data were further analyzed by fitting to Rehm–Weller and Marcus theory models in order to provide a theoretical framework for understanding and predicting electron transfer kinetics.

1. Introduction

Solvents are vitally important for chemical processing and chemical reactions.[1] They actively govern reaction rates, pathways, and equilibrium by adjusting solvation, stabilization, and diffusion of different species. Without understanding solvent effects, it is hard to predict the kinetics and thermodynamics of reactions.[2] However, the extensive use of conventional organic solvents, especially volatile solvents (*e.g.*, dichloromethane) and petroleum derived hydrocarbons (*e.g.*, toluene), poses a significant problem.[3] Their toxicity and environmental persistence, combined with high cost, have driven a need to develop greener alternative solvents. Besides this, many organic solvents are extracted from non-renewable resources, which creates a further concern.[4,5]

Deep eutectic solvents (DESs) were introduced by Abbott and co-workers in 2004.[6] They are characterized by relatively low melting points and can be easily synthesized by combining a hydrogen bond donor (HBD) and a hydrogen bond acceptor (HBA) under constant heating and stirring. Unlike many conventional solvents, their preparation does not require additional purification steps such as distillation or recrystallization.[7] The bypassing of these energy and resource intensive steps limits chemical waste and energy usage and diminishes the use of auxiliary solvents, thereby contributing to the green and sustainable nature of DESs and allowing them to function as alternatives to conventional solvents in chemical and industrial use. Since DESs show similar physicochemical properties to ionic liquids (ILs), DESs are often substituted for ILs in different applications.[8] Finally, DESs are non-volatile in nature thus making their storage very convenient.[9]

Despite similarities, DESs and ILs are markedly different in terms of their preparation and chemical constituents. ILs are formed by the combination of cations and anions, and their syntheses often require high temperatures and extended reaction times.[10] In addition, synthesis of ILs typically involves multiple steps, including cation formation followed by anion exchange. Finally, ILs are often volatile, flammable, and/or toxic, which raises significant safety and environmental concerns.[11]

In contrast, DESs offer several advantages over ILs. First, the non-toxic HBA and HBD can be used; many HBD and HBA are bio-based or inspired by naturally occurring metabolites.[12] This makes DESs environmentally friendly and well-suited for green chemistry applications. Moreover, their synthesis is generally straightforward, involving only the mixing of components followed by heating and stirring for a few hours.[12] Importantly, purification can be completed on the individual, solid HBD and HBA before DES formation.

The unique physicochemical properties of DESs, such as their polarity, low volatility, and extensive hydrogen bonding networks, make them attractive media for chemical reactions. These features are important in photochemical processes, such as photoinduced electron transfer (PET), where an electron is

---

[a] *Department of Chemistry, Binghamton University, Binghamton, New York, 13902, USA. E-mail: jswierk@binghamton.edu*

[b] *Department of Mechanical Engineering, Binghamton University, Binghamton, New York, 13902, USA*

transferred from an excited-state molecule to an acceptor molecule, leading to emission quenching and reduced emission.[13] The tunable solvation environment provided by DESs allows the optimization of PET dynamics by stabilizing charge transfer states and dictating reaction kinetics.[14] For example, the polarity and viscosity of DESs can affect the reorganization energy and charge separation efficiency in PET processes.

Electron transfer in ionic liquids (ILs) has been thoroughly investigated over the last two decades,[15–26] whereas there is significantly less work on electron transfer in DESs. Pandey and coworkers explored charge transfer through fluorescence quenching with a variety of fluorophores in DESs[27–30] but only reported quenching rate constants and did not investigate electron transfer within a theoretical framework. A variety of studies have focused on electron transfer in DESs using electrochemical methods but only reported rates of electron transfer.[31–37] Chang, Li and coworkers used computational methods to explore charge transfer from DESs to SO_2 and examined how the DESs stabilized the reduced SO_2.[38] Burda and Sangoro used femtosecond TAS and ionic conductivity to probe the eutectic composition of ethaline and characterize charge transport through the DES.[39] Finally, Smith and Goeltz demonstrated that the choice of HBA could be used to shift the potential for oxidation of a catechol-based DES that exhibited proton-coupled electron transfer.[40]

Understanding electron transfer in DESs is essential for both understanding fundamental electron transfer dynamics and rationally designing DESs for advanced applications in photocatalysis, solar energy conversion, and sensors. However, significant knowledge gaps persist, specifically in the photophysics of chromophores in DESs, the measurement of electron transfer rates, and the application of foundational theories like those of Rehm–Weller and Marcus to DES systems. To address these knowledge gaps, we investigated aqueous DES mixtures on three key aspects: the photophysics of $[Ru(bpy)_3]^{2+}$, the correlation between experimental and theoretical electron transfer rates, and the applicability of Rehm–Weller and Marcus theories in these neoteric solvents.

2. Experimental

2.1 Materials

For this study, choline chloride (>99%), ethylene glycol (>99%), tris(2,2′-bipyridine)ruthenium(II) hexafluorophosphate $[Ru(bpy)_3]^{2+}$ (>97%), methyl viologen dichloride hydrate (MV, >98%), benzyl viologen dichloride (BV, >97%), and ethyl viologen dibromide (EV, >99%) were purchased from Sigma-Aldrich. 1,1′-Diphenyl-[4,4′-bipyridine]-1,1′-diium chloride (DPV, >97%) and 1,1′-diheptyl-4,4′-bipyridinium dibromide (DHB, >98%) were purchased from TCI America. All these reagents were used as received without any further purification.

2,11-Dimethyl-6,7-dihydrodipyrido[1,2-*a*:2′,1′-c]pyrazinediium dibromide (DMPP-DB), 2,12-dimethyl-7,8-dihydro-6Ff-dipyrido-[l,2-*a*:2′,l′-*c*]-[l,4]diazepinium dibromide (DMDHP-DB), 1,1′,4,4′-tetramethyl-2,2′-bipyridinium diiodide ($TMBP-I_2$), and 6,7,8,9-tetrahydro-2,13-dimethyldipyrido ⟨1,2-*a*:2′,1′-*c*⟩ ⟨1,4⟩ diazocinediium dibromide (THDDP-DB) were prepared according to literature procedures (SI).[41,42]

2.2 Preparation and characterization of ethaline/water mixtures

For the preparation of ethaline, a DES composed of choline chloride and ethylene glycol, a published procedure was followed.[43] Choline chloride and ethylene glycol were mixed in a 1 : 2 ratio in a round bottom flask, heated, and stirred for 1 hour at 80 °C. A transparent, homogeneous and shelf stable DES was obtained. The pure ethaline DES was then subdivided into seven DES/water mixtures: 0%, 10%, 30%, 50%, 70%, 90%, and 100% water. The DES and aqueous DES mixtures were then stored in a glass desiccator to minimize moisture exposure.

Viscosity measurements were conducted using an in-house Cannon–Fenske viscometer and a TA Discovery HR30 rheometer. The redox potentials ($E_{1/2}$) of $[Ru(bpy)_3]^{2+}$ and various quenchers in the DES/water mixtures were measured using cyclic voltammetry. A BioLogic SP-50 potentiostat was used along with glassy carbon as the working electrode, aqueous silver–silver chloride as the reference electrode, and a platinum wire as the counter electrode.

2.3 Quenching studies

Emission and absorption measurements were carried out using a Shimadzu RF-6000 spectrofluorophotometer and a Shimadzu UV-2600 spectrophotometer, respectively. For Stern–Volmer emission (phosphorescence) quenching studies, a 0.026 mM $[Ru(bpy)_3]^{2+}$ solution was prepared. Similarly, for all nine quenchers, a series of stock solutions were prepared and used for electron transfer analysis. A four-sided transparent cuvette was used for analysis and each sample was purged with nitrogen gas for at least 30 minutes to remove any dissolved oxygen. For emission lifetime measurements, a 0.026 mM solution of $[Ru(bpy)_3]^{2+}$ in the DES/water mixtures was prepared and the emission lifetime (τ) was measured using transient emission spectroscopy, as previously described in ref. 44.

3. Results and discussion

3.1 Viscosity of DES/water mixtures

The viscosities of the DES/water mixtures were measured (Table 1) and modelled using the Grunberg–Nissan model.[45] The model used the ideal logarithmic mixing rule, mole fraction of ethaline and water, and an interaction term, G_{12}, which indicates deviation from ideality (SI).[45] The mole fractions, calculated from the volumetric percentages and densities of the ethaline/water mixtures, are listed in Table S1. The experimental viscosities were used in eqn (S1) to compute G_{12}, which was optimized using a non-linear least square regression to minimize the error between the experimental and predicted viscosities.

The resulting G_{12} value of 4.052 is positive, indicating significant non-ideal behavior in the ethaline–water mixtures. This non-ideality originates from the strength and nature of

Table 1 Emission quantum yield (Φ), lifetime (τ), and radiative and non-radiative decay constants in all ethaline mixtures. [The percent standard error in η is < 0.2%, and the standard deviation in Φ is < 0.223]

DES	η (Pa s)	$k_D \times 10^9$ (M^{-1} s^{-1})	τ (ns)	Φ	$k_r \times 10^4$ (s^{-1})	$k_{nr} \times 10^6$ (s^{-1})
0	0.000991	6.67	222	0.063[a]	28.4	4.22
10	0.001092	6.05	561	0.030	5.37	1.73
30	0.00188	3.52	647	0.027	4.18	1.50
50	0.00368	1.80	762	0.027	3.61	1.28
70	0.00853	0.775	785	0.032	4.03	1.23
90	0.0237	0.279	861	0.031	3.57	1.13
100	0.0326	0.203	928	0.031	3.30	1.04

[a] Literature value of Φ of $Ru(Bpy)_3{}^{2+}$ in water.[50]

intermolecular interactions (*e.g.*, hydrogen bonding, van der Waals forces, and ionic interactions) between the components.[46]

These interactions result in increased structural rigidity and higher viscosity. This effect is most pronounced at the 50% DES mixture, where G_{12} reaches a maximum (4.447), reflecting a denser hydrogen bond network and more persistent coordination environments, which increases resistance to flow and therefore causes the strong, nonlinear rise in viscosity, characterized by a sharp rise at high DES concentrations. The Grunberg–Nissan model confirms that the viscosity increase is not a linear sum of the pure component viscosities but is supplemented by strong intermolecular interactions, as revealed by the positive G_{12} value.[47]

3.2 Photophysical characterization of $[Ru(bpy)_3]^{2+}$

The emission lifetime (τ) of $[Ru(bpy)_3]^{2+}$ was measured in the ethaline/water mixtures (Fig. S5 and Table 1). The emission lifetime of $[Ru(bpy)_3]^{2+}$ increased from 222 ns in 0% DES to 928 ns in 100% DES. This increased τ reflects slower relaxation processes and stabilization of the excited state as the solvent becomes more viscous.[48] The quantum yield of emission (Φ) for $[Ru(bpy)_3]^{2+}$ was also calculated[49] using eqn (1) in the DES mixtures (Table 1). $[Ru(bpy)_3]^{2+}$ in 0% DES was used as a standard.[50]

$$\Phi = \Phi_{\text{std}}\left[\frac{I_x/A_x}{I_{\text{std}}/A_{\text{std}}}\right] \tag{1}$$

where Φ stands for the quantum yield of emission, Φ_{std}, I_{std}, and A_{std} are the standard quantum yield, integrated area of the standard emission curve, and absorbance at an excitation wavelength of the standard, respectively and I_x and A_x represent the integrated area of the sample and absorbance at an excitation wavelength of the sample, respectively.

The Φ values are 2–3% in all ethaline mixtures suggesting reduced emission efficiency per absorbed photon. These low Φ values agree with previous studies,[51,52] and are attributed to the involvement of the non-emissive metal-centered, d–d state (^{3}MC).[53] The ^{3}MC state introduces an efficient nonradiative decay pathway that competes directly with emission from the ^{3}MLCT state. Even though the ^{3}MC level lies at higher energy and its steady state population remains negligible, thermally assisted access to this surface allows a fraction of the ^{3}MLCT population to cross into ^{3}MC.[54] Because the ^{3}MC state relaxes to the ground state on an ultrafast timescale, any population that reaches it is effectively removed from the emissive manifold.[55] This nonradiative leakage pathway lowers the fraction of molecules that decay radiatively, leading to a reduced Φ.

Radiative (k_r) and non-radiative (k_{nr}) decay constants were calculated using eqn (2a) and (2b) and the results are tabulated in Table 1.[56]

$$k_r = \frac{\Phi}{\tau} \tag{2a}$$

$$k_{nr} = \frac{(1-\Phi)}{\tau} \tag{2b}$$

In eqn (2a) and (2b), Φ and τ represent the quantum yield of emission and emission lifetime. Both k_r and k_{nr} values dropped by a factor of nine and four, respectively, as the ethaline content was increased. These comparatively larger values of k_{nr} as compared to k_r suggest that k_{nr} is the primary decay mechanism in this case. The decrease in k_{nr} is because of increasing viscosity and the structural rigidity of ethaline mixtures, which ultimately suppress the k_{nr}. On the other hand, the decrease in the k_r is attributed to the unique solvodynamic properties of the ethaline mixtures. The combined effects of a strong hydrogen-bonding network, high ionic strength, and an enhanced refractive index create a restrictive microenvironment that perturbs the emissive ^{3}MLCT state. This environment restricts the electron density redistribution necessary for the radiative transition, thereby attenuating the transition dipole moment and greatly reducing k_r. The Φ, which is the fraction of excited molecules that decay *via* light emission, remains stable or shows a slight decline.

Initially, it is somewhat surprising that the emission lifetime increases while Φ and k_r decreases. It is important to note, however, that $\tau = (k_r + k_{nr})^{-1}$. Because k_{nr} is the primary excited state decay pathway and is ~2 orders of magnitude larger than k_r, the decrease in k_{nr} has a more substantial impact on τ and a longer lifetime is observed. In contrast, Φ has more direct dependence on k_r so a decrease in this rate constant leads to a smaller value of Φ.

A deeper analysis of $[Ru(bpy)_3]^{2+}$ photophysics in the ethaline/water mixtures was performed by fitting the emission spectra (Fig. S8) using a one mode Franck–Condon analysis.[57] This offers a way to probe how the DES/water mixtures influence the metal-to-ligand charge transfer (MLCT) excited state dynamics as the solvent environment transitions from pure water to pure DESs.

The analysis of the emission spectra yielded six key photophysical parameters (Table 2), which were used to calculate four additional parameters: the activation barrier (ΔE_{act}) for ^{3}MLCT to ^{3}MC transition, the solvent reorganization energy (λ_s), and the inner reorganization energy (λ_i). The meaning and significance of these parameters are as follows:

- E_{0-0} (0–0 transition energy): this represents the energy of the MLCT transition between the lowest vibrational levels of the

Table 2 The spectral fitting parameters of $[\mathrm{Ru(bpy)_3}]^{2+}$ in all ethaline mixtures

DES %	E_{0-0} (cm^{-1})	$\hbar w_\mathrm{m}$ (cm^{-1})	$\Delta\nu_{1/2}$ (cm^{-1})	S_M	γ_0	ln(F_calc)	λ_s (eV)	λ_i (eV)	λ (eV)	ΔE_act	E (Ru^{3+}/Ru^{2+}) V *vs.* Ag/AgCl
0	16 405	1447	1851	0.7598	1.7027	−28.40	0.376	0.136	0.512	0.436	−0.920
10	16 377	1472	1860	0.7482	1.6994	−28.02	0.380	0.137	0.517	0.459	−0.916
30	16 357	1479	1845	0.7306	1.7171	−28.10	0.374	0.134	0.508	0.462	−0.914
50	16 342	1474	1839	0.7151	1.7410	−28.37	0.371	0.131	0.502	0.466	−0.912
70	16 321	1484	1824	0.7106	1.7391	−28.23	0.365	0.131	0.496	0.467	−0.909
90	16 284	1489	1814	0.7100	1.7345	−28.09	0.361	0.131	0.492	0.470	−0.905
100	16 261	1488	1806	0.6971	1.7522	−28.26	0.358	0.129	0.487	0.472	−0.902

ground and excited states. It reflects how the solvent stabilizes the charge-separated excited state.

- $\hbar w_\mathrm{m}$ (average vibrational mode energy): this indicates the energy of the dominant molecular vibration coupled to the electronic transition, providing a measure of vibronic coupling strength.
- $\Delta\nu_{1/2}$ (spectral width) and λ_s (solvent reorganization energy): the full width at half maximum ($\Delta\nu_{1/2}$) of the spectrum reports on the broadening due to solvent interactions. It is directly used to calculate λ_s, which quantifies the energy required for the solvent to reorganize around the newly created excited-state dipole.
- S_M (Huang–Rhys factor) and λ_i (inner reorganization energy): the Huang–Rhys factor (S_M) describes the strength of coupling between the electronic transition and specific molecular vibrations. The inner reorganization energy (λ_i) is derived from these factors and represents the energy required to distort the molecular structure upon excitation.
- ln(F_calc) (the Franck–Condon factor or Frank–Condon vibrational overlap term) and γ_0 (Linewidth parameter): the Franck–Condon factor ln (F_calc) governs the probability of the non-radiative transition back to the ground state, linking directly to the energy gap law. The γ_0 parameter accounts for the Gaussian broadening of individual vibronic lines.

As the percentage of DESs increases, the E_{0-0} values decrease steadily indicating a reduction in energy gap (Table 2). As the ground state potential remains constant (see below), this indicates a stabilization of the ^{3}MLCT state relative to the ground state with increasing ethaline content. Fig. 2 shows the relationship between k_nr and E_{0-0}, which exhibits a positive slope (0.0079).[58]

The positive slope between k_nr and E_{0-0} indicates that the non-radiative decay of $[\mathrm{Ru(bpy)_3}]^{2+}$ in ethaline/water mixtures is not governed by direct decay to the ground state but by a thermally activated decay (TAD) mechanism.[53] In this mechanism, the molecule gains thermal energy from the surroundings to reach a higher energy, non-emissive metal-centered, d–d state (^{3}MC) from the emissive ^{3}MLCT. The metal-centered state then rapidly decays to the ground state.[59,60] This transition requires crossing an activation barrier (ΔE_act) that must be thermally overcome for the population transfer from ^{3}MLCT to the ^{3}MC state.[61] TAD can be modelled by:[62]

$$k_\mathrm{nr} = k_0 \exp\left(-\frac{\Delta E_\mathrm{act}}{k_\mathrm{B}T}\right) \tag{3a}$$

$$\ln k_\mathrm{nr} = \ln k_0 - \frac{\Delta E_\mathrm{act}}{k_\mathrm{B}T} \tag{3b}$$

$$\Delta E_\mathrm{act} = (\ln k_0 - \ln k_\mathrm{nr}) \times k_\mathrm{B}T \tag{3c}$$

where k_0 is the pre-exponential factor for crossing the activation barrier, ΔE_act is the activation barrier, k_B is the Boltzmann constant, and T represents the room temperature at which the experiments were performed.

For Ru(II) complexes, k_0 is typically $\sim 10^{13}$–10^{14} s^{-1}.[63] This model allows the calculation of ΔE_act at room temperature by using eqn (3c). The calculated ΔE_act values are given in Table 2. As the content of ethaline increases, the value of ΔE_act also increases. This can be attributed to ethaline's moderate polarity[9] and hydrogen bonding,[64] which can stabilize the ^{3}MLCT state (demonstrated by the decreasing value E_{0-0}). In turn, this increases the barrier (ΔE_act) to the ^{3}MC state and ultimately reduces k_nr. The increase in $\hbar w_\mathrm{m}$ values with increasing DES concentration also indicates that the ethaline's hydrogen bond donors are restricting the bipyridine vibrational modes. This may be *via* a specific interaction such as bonding between the OH groups of ethylene glycol and the nitrogen atoms on bipyridine.[65]

We can also calculate the solvent reorganization energy for the excited state, λ_s, from the $\Delta\nu_{1/2}$ of the charge-transfer emission band, using a modified Gaussian Marcus–Hush equation (eqn (4)).[66]

$$\lambda_\mathrm{s} = \frac{(\Delta\nu_{1/2})^2}{\left[8\ln(2) \times \dfrac{k_\mathrm{B}T}{hc}\right]} \tag{4}$$

In this equation, k_B is the Boltzmann constant, h is Planck's constant, and c is the speed of light. Vath *et al.* used this approach to extract λ_s values from CT absorption/emission bandwidths across different solvents and temperatures.[67] Their methodology justifies linking the observed thermal broadening directly to the solvent outer-sphere reorganization energy. Both $\Delta\nu_{1/2}$ and λ_s values decrease as the solvent goes from a water-rich to an Ethaline-rich environment, which can be linked to the ethaline mixture's increasing viscosity. The increased viscosity can restrict the solvent's reorientation and reduce thermal broadening.

We can also calculate the inner reorganization energy (λ_i) using S_M, which quantifies the ratio of structural distortion by identifying the shift between ground and excited MLCT state potential energy surfaces along vibrational modes. λ_i is the energy required for structural rearrangement within a molecule as it moves from the excited state to the ground state during emission and can be calculated by using eqn (5).[68]

$$\lambda_i = S_M \times \hbar w_m \tag{5}$$

In eqn (5), S_M stands for the Huang–Rhys Factor and $\hbar w_m$ stands for the average vibrational mode energy.

For $[Ru(bpy)_3]^{2+}$, λ_i basically corresponds to vibrations of the bipyridine (bpy) ligand, such as ring stretches and Ru–N bond stretches, that are associated with electron transfer processes.[69] The decrease in S_M leads to a decrease in λ_i values and indicates less of a shift between ground and excited state potential energy surfaces with increasing DES concentration. This implies that the bipyridine ligands encounter less geometric distortion in the MLCT state as the ethaline's content is being increased. We suggest that this stems from ethaline's hydrogen bonding stabilizing the bpy^- moiety and thus helps delocalize the charge and limits structural changes. The calculation of solvent reorganization (λ_s) and inner reorganization energy (λ_i) allows the quantification of total reorganization energy (λ) for emission by the following relationship:[70,71] $\lambda = \lambda_s + \lambda_i$. As expected, λ also decreases linearly with increasing DES concentration (Table 2).

The plot between S_M and E_{0-0} shows a linear trend (Fig. 3), which indicates a systematic relationship between the energy gap of the MLCT excited state and the degree of vibronic coupling. This is influenced by the solvent environment. The combined influence exerted by the solvent on E_{0-0} (electronic stabilization) and S_M (vibronic coupling) is evident as the increase in ethaline content enhances both structural solvation and stabilizing dipole–dipole and hydrogen bonding interactions. This linearity also highlights the gradual transition from water's polar and dynamic solvation to ethaline's ionic and viscous environment, which stabilizes the ^{3}MLCT state (lower E_{0-0}) and reduces bpy distortion (lower S_M). The observed correlation between $\ln(k_{nr})$ and E_{0-0} should therefore not be interpreted as evidence of rigid, parallel shifts of the potential energy surfaces. Rather, E_{0-0} reflects stabilization of the emissive ^{3}MLCT minimum, while k_{nr} is governed by the barrier-controlled access to the ^{3}MC surface, which is strongly influenced by local solvation, viscosity, and hydrogen-bond interactions characteristic of deep eutectic solvents.

The Frank–Condon factor which is also called the Frank–Condon vibrational overlap term, $\ln(F_{calc})$, counts the vibrational overlap between the ground and excited states during the MLCT emission processes. The negative values observed for $\ln(F_{calc})$ mean a small Franck–Condon factor and indicate poor vibrational overlap between the ground and excited states. This poor overlap greatly suppresses k_{nr} according to the energy gap law, which is also the primary factor for prolonging τ. This effect is reinforced in ethaline-rich mixtures, where strong ionic and hydrogen bonding interactions rigidify the solvation shell and distort the excited-state geometry,[14] further diminishing the vibrational overlap and potentially perturbing the electronic transition dipole strength.

The plot of $\ln(F_{calc})$ as a function of $\ln(k_{nr})$ is shown in Fig. 4.

This plot illustrates the energy gap law, showing how the rate of non-radiative decay rises in proportion to the Franck–Condon factor, a measure of vibronic overlap that governs this process. In the energy gap law, k_{nr} is modelled as follows:

$$k_{nr} \approx AF_{calc} \tag{6a}$$

$$\ln(k_{nr}) \approx \ln A + \ln F_{calc} \tag{6b}$$

In this case, the slope is set to 1, as k_{nr} is directly proportional to F_{calc} and the intercept is $\ln(A)$, where A is the pre-exponential factor associated with vibrationally induced electronic coupling.[56] From the slope of Fig. 4, $\ln(A) \approx 42.45$ and thus $A \approx 2.73 \times 10^{18}$ s^{-1}, which suggests that $\ln(F_{calc})$ accounts for both the vibrational overlap and the energy barrier to the ^{3}MC state. This extremely large coupling factor ($\sim 10^{18}$ s^{-1}) suggests strong electronic coupling between ^{3}MLCT and ^{3}MC surfaces. This magnitude is above the typical vibrational frequency range of $\sim 10^{12}$–10^{14} for MLCT complexes like $[Ru(bpy)_3]^{2+}$ and further confirms the idea that the nonradiative decay does not follow a simple energy gap law pathway to the ground state.[58,72] Instead, the excited state deactivation proceeds through a thermally activated transition involving the ^{3}MLCT to ^{3}MC crossing. Finally, we note that in the present analysis A should not be interpreted as a bare vibrational attempt frequency. In our formulation, F_{calc} is not a pure Franck–Condon overlap term, but an effective factor that also incorporates the energetic barrier and multidimensional nuclear reorganization associated with accessing the ^{3}MLCT to ^{3}MC crossing region. Consequently, the pre-factor A represents an effective coupling parameter that absorbs electronic coupling, density of accepting states, and deviations from a single-mode harmonic approximation. Similar large pre-factors are also known in the photophysical literature as well.[56,72]

The Gaussian linewidth parameter, γ_0, reports on the emission band broadening for $[Ru(bpy)_3]^{2+}$ in ethaline mixtures coming from low frequency vibrational modes and solvation inhomogeneity. This can be calculated using eqn (7):[58]

$$\gamma_0 = \ln\left(\frac{E_0}{S_M \times \hbar w_m}\right) - 1 \tag{7}$$

The values of γ_0 are gradually increasing with increased DES content (Table 2), indicating enhanced ionic and hydrogen bonding interactions with the solvent. This also indicates increasing static disorder and low frequency mode coupling, which results in broadening of vibronic bands.

Finally, the excited state potentials of $[Ru(bpy)_3]^{2+}$ in all ethaline/water mixtures were calculated using the following Rehm–Weller relationship.[73]

$$E(A^+/A^*) = E(A^+/A^-) - E_{0-0} \tag{8}$$

In this equation, $E(A^+/A^-)$ corresponds to the ground state reduction potential and E_{0-0} is the difference in energy between ground and excited state energies. E_{0-0} can be calculated from emission spectra fitting and the values are listed in Table 2. The ground state reduction potential can be determined using cyclic voltammetry. The voltammogram of $[Ru(bpy)_3]^{2+}$ in ethaline mixtures and reduction potentials are given in Fig. S9 and Table S2, respectively. Using all these data, the excited state potentials are calculated using eqn (8) and the corresponding values are given in Table 2. We observe a slight decrease of 18 mV in the excited state potential increasing from 0% to 100% ethaline.

3.3 Photoinduced electron transfer

In order to understand electron transfer in the DES mixtures, we carried out emission quenching studies using $[Ru(bpy)_3]^{2+}$ and a series of viologens quenchers (Fig. 1). The absorbance spectra of $[Ru(bpy)_3]^{2+}$ was similar in all the DES mixtures with an absorbance maxima at ∼454 nm. The emission spectra of $[Ru(bpy)_3]^{2+}$ in all the DES mixtures, with and without quenchers, are presented in Fig. S19–S27.

The kinetics of emission quenching can be quantified using the Stern–Volmer relationship:[74]

$$\frac{I_0}{I} = 1 + K_{sv}[Q] \tag{9}$$

$$k_q = \frac{K_{sv}}{\tau_0} \tag{10}$$

Here, I_0 is the emission intensity in the absence of a quencher, I is the emission intensity in the presence of a quencher, Q is the concentration of a quencher, τ_0 is the lifetime of the chromophore, K_{sv} is the Stern–Volmer constant (L mol^{-1}), and k_q is the quenching rate constant (M^{-1} s^{-1}). K_{sv} can be derived by plotting I_0/I vs. [Q] (Fig. S28–S36 and Table 3). The quenching rate constants (k_q) were also calculated and are given in Table 3. In the DES mixtures, the k_q values are between 3.8×10^6 and 2.9×10^8 M^{-1} s^{-1}, which are smaller compared to water and other conventional solvents. When compared to quenching in ionic liquids, the values of k_q in ethaline/water mixtures are similar or larger.[75–80]

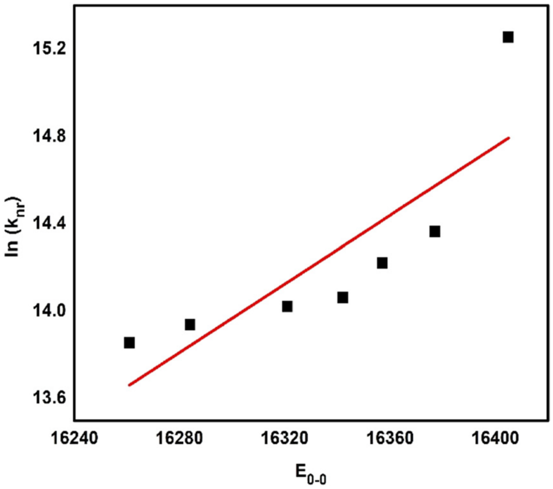

Fig. 2 The plot of nonradiative decay ln (k_{nr}) *vs.* transition energy (E_{0-0}) with a slope of $7.86 \times 10^{-3} \pm 2.30 \times 10^{-3}$, a y-intercept of -114.123 ± 37.596 and a R^2 of 0.6998, based on the data given in Table 2.

To better understand the k_q values, the diffusion limited rate constants (k_D) were calculated using the Smoluchowski equation:[22]

$$k_D = \frac{8000RT}{3\eta} \tag{11}$$

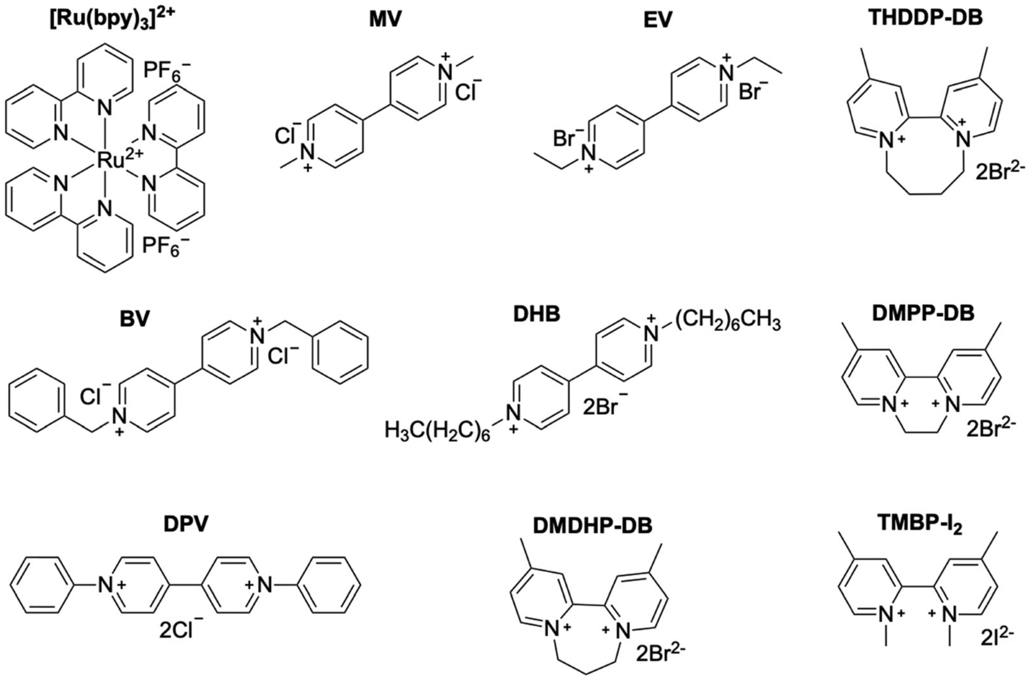

Fig. 1 Photosensitizers and quenchers used in the study. $[Ru(bpy)_3]^{2+}$, MV, EV, THDDP-DB, BV, DHB, DMPP-DB, DPV, DMDHP-DB, and $TMBP-I_2$.

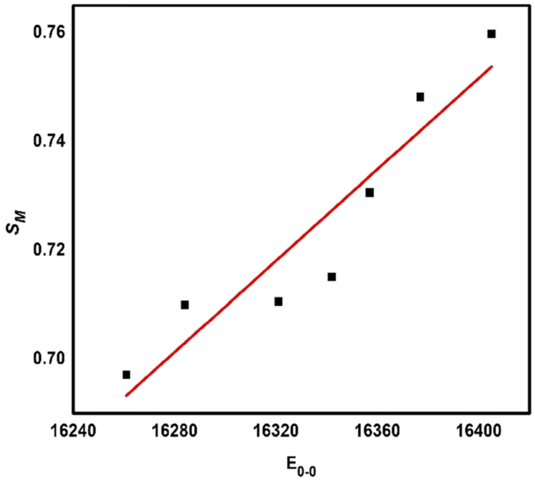

Fig. 3 The plot of Huang–Rhys factor (S_M) *vs.* transition energy (E_{0-0}) with a slope of 4.20 × 10^{-4} ± 6.81 × 10^{-5}, a *y*-intercept of −6.135 ± 1.113 and a R^2 of 0.8836, based on the data given in Table 2.

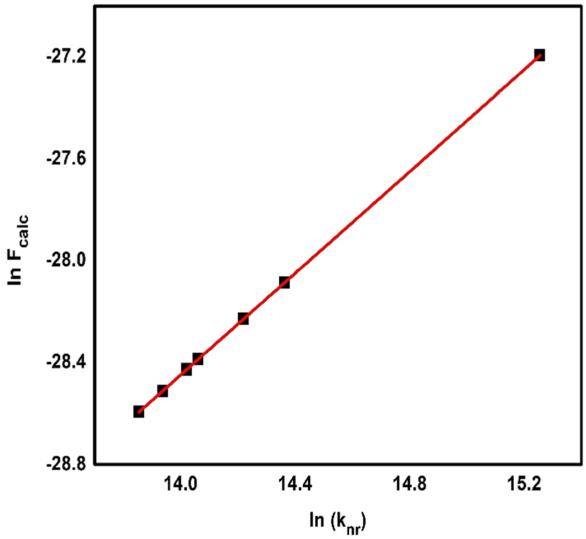

Fig. 4 The plot of Franck–Condon overlap factor ln (F_{calc}) *vs.* nonradiative decay ln (k_{nr}) with a slope fixed at 1, a *y*-intercept of −42.45 ± 9.24 × 10^{-14} and a R^2 of 1, based on the data given in Table 2.

Here, R is the ideal gas constant (J K^{-1} mol^{-1}), T is the temperature (K), and η is the viscosity (Pa s). Experimental viscosities and diffusion limited rate constant (k_D) of aqueous DES mixtures are given in Table 1. As expected, with increasing viscosity, the value of k_D decreases (Fig. 5).

The data reveal that k_q values decrease as the DES concentration is increased. This could be because of an increase in the overall viscosities of DES mixtures. Alternatively, a decrease in dipolarity or polarizability of the solvent with increasing DES concentration may hinder or slow down the charge transfer between the quenchers and $[Ru(bpy)_3]^{2+}$.[81] Water molecules disrupt the hydrogen bond network of ethaline, which alters the molecular arrangement and weakens cohesive forces, leading to a reduction in solvent viscosity with increasing water.[82] Due to the high viscosity of DES mixtures, slower solvation might create a more constrained environment around the chromophore. Consequently, this may influence the accessibility of the molecules acting as electron acceptors or donors in the electron transfer process, potentially leading to decreased rates of electron transfer.[83] Except for DPV, the k_q values for all DES mixtures and quenchers were less than k_D, demonstrating that electron transfer was not diffusion controlled. These comparatively smaller k_q values when compared to k_D are typical for viscous liquids.[23,84] This trend can be attributed to variance between the recorded "macroviscosity" of each DES mixture and the "macroviscosity" in the immediate vicinity of the donor–acceptor pair. While bulk viscosity values (Table 1) obtained experimentally show the average resistance to flow for the entire ethaline/water mixture, they do not necessarily show the local dynamic environment immediately surrounding the solute (donor–acceptor pair) molecule. Especially, in DESs, hydrogen bonding networks, ionic clustering, and microheterogeneity can create domains in which solute molecules experience a viscosity that differs greatly as compared to the bulk.[14] As a result, in such cases, diffusion, solvation, and electron transfer processes are controlled by local (micro)viscosity rather than the bulk viscosity.[85] Therefore, the viscosity of the DES mixtures (Table 1) may not report the local environment and diffusion of donor–acceptor pairs within the DES mixtures.[23]

The observed k_q data for the electron transfer between $[Ru(bpy)_3]^{2+}$ and MV in the ethaline DES (∼1.3 × 10^8 L mol^{-1} s^{-1}) can be placed into the context by comparison with literature values in other solvent environments. In conventional molecular–solvent media such as acetonitrile and water, significantly higher rates have been documented (for example, water: ∼1.7 × 10^9 L mol^{-1} s^{-1}; buffer: ∼4.6 × 10^8 L mol^{-1} s^{-1}), indicating nearly diffusion-controlled or only modestly solvent-hindered quenching.[86,87] In contrast, ionic-liquids (IL) frequently show much lower k_q values (in the 10^7 L mol^{-1} s^{-1} range) despite their relatively high viscosity, which is attributed to suppressed diffusion, strong ion-pairing and structured solvation shells.[88–90] The somewhat higher k_q in the neat DES system lies between the IL and molecular-solvent extremes, indicating that while the DES network imposes mobility restrictions (*via* high viscosity, extensive hydrogen-bonding and ionic framework) it still allows more efficient donor–acceptor encounters compared with classic ILs.

3.4 Rehm–Weller analysis and Marcus theory

Using the k_q values determined from Stern–Volmer analysis, the electron transfer can be modelled by both Rehm–Weller[91] and Marcus theories.[92] The Rehm–Weller analysis gives a simple thermodynamic model to predict if an electron transfer reaction involving an excited molecule is energetically feasible. By comparing the energy of the excited state to the redox potentials of the reacting molecules, it calculates the free energy change (ΔG) for the process.[91] Marcus theory on the other hand is a kinetic model and predicts that the rate of an electron transfer reaction does not increase indefinitely with increased thermodynamic driving forces ($-\Delta G^0$), but instead

Table 3 Stern–Volmer constants (K_{sv}) and quenching rate constant (k_q) of quenchers in $[Ru(bpy)_3]^{2+}$ in all DES mixtures

	MV	BV	EV	DPV	DHB	DMPP-DB	DMDHP-DB	THDDP-DB	TMBP-I_2
DES%	K_{sv} (L mol^{-1})								
0	322	619	404	1061	648	415.3	208.2	52.87	18.61
10	1223	1222	1059	1881	1356	1051.2	393.03	177.05	45.98
30	950	1058	1008	1712	1229	982.7	387.5	146.5	40.15
50	730	797	711	1359	817	840.4	281.4	103.2	35.08
70	416	415	443	1194	492	460.7	171.15	62.3	25.33
90	233	189	209	755	214	185.7	74.51	36.7	14.04
100	115.76	110.22	138.68	270.1	124.61	110.1	38.2	35.5	5.96
	$k_q \times 10^9$ (L mol^{-1} s^{-1})								
0	1.45	2.79	1.82	4.78	2.92	1.87	0.94	0.24	0.084
10	2.18	2.18	1.89	3.35	2.42	1.87	0.7	0.32	0.082
30	1.47	1.64	1.56	2.65	1.9	1.52	0.59	0.25	0.062
50	0.96	1.05	0.93	1.78	1.07	1.10	0.37	0.135	0.046
70	0.53	0.53	0.56	1.52	0.63	0.59	0.22	0.0079	0.032
90	0.27	0.22	0.24	0.88	0.25	0.22	0.087	0.0043	0.007
100	0.13	0.12	0.15	0.29	0.14	0.12	0.042	0.0038	0.006

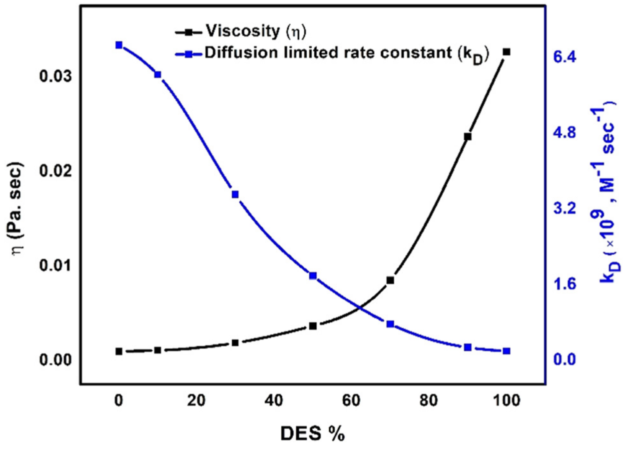

Fig. 5 The plot of viscosity (η) and diffusion limited rate constant (k_D) as a function of DES concentration.

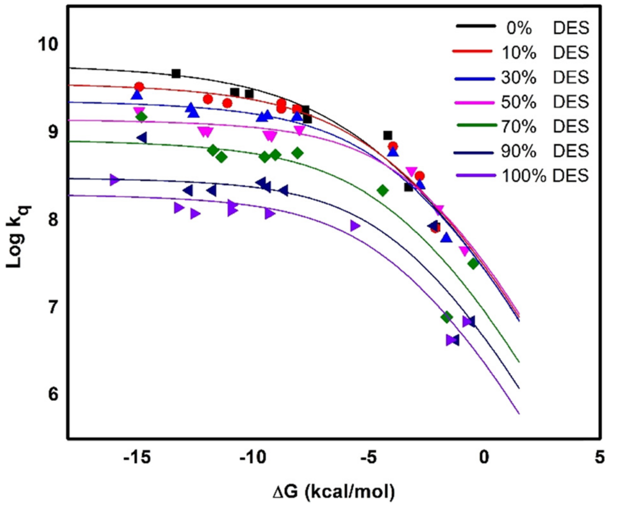

Fig. 6 Experimental electron transfer data plotted using the Rehm–Weller model for thermodynamic analysis.

follows a parabolic curve.[92] This means that the rate initially increases in the normal region before reaching a maximum and then decreasing in the inverted region as the driving force becomes increasingly larger.[92]

The electron transfer data in Table 3 was fit using both Rehm–Weller and Marcus analyses, with the corresponding plots shown in Fig. 6 and Fig. S37. Individual plots are shown in Fig. S38 and S39. In the Rehm–Weller equation,[22]

$$\Delta G_{et} = 23.06(E^{D}_{ox} - E^{A}_{red}) - E_{0,0} - S \qquad (12)$$

where E^{D}_{ox}, E^{A}_{red}, $E_{0,0}$, and S are the oxidation potential of the donor, the reduction potential of the acceptor, the excited state energy of the acceptor, and a solvent-dependent Coulombic stabilization of the radical ion pair formed after electron transfer.

A plot of log k_q *vs.* ΔG yields information about k^{max}_{diff}, which represents the diffusion-controlled electron transfer limit, and λ, which is the total reorganization energy for electron transfer. Together, the two parameters give an idea about how much structural and solvent reorientation is required for electron transfer to take place. Also, the solvation or coulombic stabilization factor, S reports on if ion-pair stabilization in solvent impacts the observed rates of electron transfer. The calculated ΔG_{ET} values are listed in Table S3 of the SI file and ΔG_{ET} data reveal a systematic influence of the DES composition on photoinduced electron transfer. For highly reducible electron acceptors, such as DPV and DHB, ΔG_{ET} remains highly negative across all DES mixtures, indicating that the corresponding electron transfer reactions are strongly exergonic and likely occur near the diffusion-controlled limit. In contrast, for weaker acceptors such as THDDP-DB and TMBP–I_2, ΔG_{ET} values approach zero at low DES content and become progressively more negative with increasing DES fraction, suggesting that the ionic environment of the DES enhances charge separation by stabilizing the radical ion pair. The parameters derived from log k_q *vs.* ΔG plot are given in Table 4.

Table 4 Electron transfer parameters derived from Rehm–Weller plots

DES%	λ (kcal mol^{-1})	λ (eV)	$k_{\text{diff}}^{\text{max}} \times 10^{11}$ (M^{-1} s^{-1})	S
0	12	0.520	7.00	2.8
10	11.5	0.499	5.00	2.8
30	11	0.477	3.00	2.8
50	10.3	0.447	2.00	2.0
70	11	0.477	1.00	1.4
90	11.7	0.507	0.90	0.8
100	11.8	0.512	0.50	0.8

The λ for electron transfer exhibits a non-monotonic trend across the ethaline/water mixtures. The value of λ decreases from 12.0 kcal mol^{-1} (0% DES) to a minimum of 10.3 kcal mol^{-1} (50% DES) and then increases again to 11.8 kcal mol^{-1} (100% DES). This $\sim$14% variation reflects solvent-dependent effects on solvent reorganization and intramolecular rearrangements, driven by ethaline's increasing viscosity and ionic interactions. The minimum at 50% DES corresponds to enhanced intermolecular interactions, as evidenced by the elevated G_{12} interaction factor from the Grunberg–Nissan viscosity model, and is consistent with the non-ideal mixing discussed earlier. The subsequent rise in λ at a higher ethaline content suggests stronger hydrogen-bonding and ionic solvation in ethaline mixtures, increasing the energy required for solvent reorganization.[93,94] On the other hand, $k_{\text{diff}}^{\text{max}}$ decreases considerably with increasing ethaline content, which can be attributed to a significant increase in viscosity and reduced molecular diffusion in the ethaline-rich environment. Finally, the S factor also decreases linearly with ethaline content, showing that the ethaline's environment is partially stabilizing the charge-separated state and reducing the contribution of solvent reorganization to the driving force.

Similarly, the electron transfer data were also analysed using the Marcus equation (eqn (S2), SI).[95] ΔG for electron transfer (Table S4) shows some dependence on the ethaline content and tends to become less exergonic with increased ethaline content. A comparison between ΔG and λ data (Table S5) splits quenchers into different Marcus kinetic regions. The quenchers with less exergonic or endergonic ΔG values such as TMBP-I$_2$ ($\sim$0.01 to 0.06 eV), THDDP-DB (−0.02 to 0.01 eV) and DMDHP-DB (−0.20 to −0.04 eV) can be classified in the normal region across all ethaline compositions. These quenchers show reduced quenching efficiency because of positive or near-zero ΔG, demanding a greater driving force to approach the barrierless region. On the other hand, for quenchers such as BV, MV, EV, and DMPP-DB, the ΔG values are approaching $-\lambda$ and thus are near a barrierless reaction. In this region, experimental k_q values are approaching optimal electron transfer efficiency with nominal activation barriers. Finally, the most exergonic quenchers such as DPV (−0.46 to −0.65 eV) and DHB (−0.35 to −0.53 eV) fall in the inverted region especially at higher ethaline concentrations (90 and 100% DESs). In these solvent concentrations, $\Delta G < -\lambda$ and k_q values are decreasing, probably because of vibronic overlap, even after with a large driving force for electron transfer. This is most obvious in the 100% ethaline concentration where ΔG becomes more negative and the λ value is reduced.

Between the two models, the values of λ are in good agreement with a difference of 1–2 kcal mol^{-1} between the two models. Comparing the data for λ obtained in neat ethaline, 10.14–11.8 kcal mol^{-1}, the values in DESs are substantially smaller than the 17.7–18.5 kcal mol^{-1} range reported for Ru(bpy)-related complexes in ethanol–water mixtures, a reduction of roughly 35–43%.[86,96] The reduced λ values are mechanistically important and reflect a reduced outer-sphere (solvent) reorganization contribution.

4. Conclusions

The photophysical characterization of [Ru(bpy)$_3$]$^{2+}$ in ethaline/water mixtures demonstrates that the chromophore has a significantly stabilized ^{3}MLCT state with pronounced luminescence, extended excited state lifetimes, and suppressed nonradiative decay. These effects can be credited to the strong ionic and hydrogen bonding network of ethaline, which effectively rigidifies the chromophores and stabilize its charge transfer state.

The unique ethaline environment also influences electron transfer dynamics. The experimental data are well described by both the Rehm–Weller and Marcus models. Rehm–Weller analysis shows that the thermodynamics and intrinsic reorganization aspects of electron transfer are largely unaffected by the specific ethaline/water mixture but the rates of electron transfer are strongly controlled by the viscosity and solvation properties of ethaline, revealing a dual role of ethaline in controlling both energetics and dynamics of electron transfer. The Marcus model demonstrates a shift from the normal to the inverted region for high driving force electron transfer. The data also suggest that ethaline/solvent mixtures could be used to modulate the rate of electron transfer and introduce selectivity in the electron transfer dynamics.

The bimolecular electron transfer rate (k_q) of [Ru(bpy)$_3$]$^{2+}$ with MV in ethaline DESs (1.3×10^8 L mol^{-1} s^{-1}) is significantly higher than that in typical ILs, comparable to moderate acetonitrile values, but lower than that in water or phosphate buffer. This reflects the intermediate viscosity and structured hydrogen bonding network of ethaline, which slows diffusion relative to water but promotes efficient charge transfer through stabilization of the encounter complex. In addition, the reorganization energies obtained for the [Ru(bpy)$_3$]$^{2+}$ to MV electron transfer in neat ethaline, 10.14 and 11.8 kcal mol^{-1} from Marcus and Rehm–Weller models, are notably smaller than the values commonly reported in ethanol–water mixtures. This reduction indicates that the ethaline environment imposes a lower solvent reorganization penalty, consistent with its structured hydrogen bonded and ionic network. A smaller λ supports more efficient electron transfer once the encounter complex is formed.

The conclusions drawn in this work are strictly valid for ethaline and are expected to be most transferable to structurally similar hydrogen-bond-donor-based DESs, rather than universally applicable to all DES classes. Broadly speaking, the data demonstrate that increasing viscosity from ethaline is not solely impacting electron transfer dynamics. Instead, the solvation environment also plays a role in stabilizing the charge transfer state. In addition, it is clear that electron transfer behaviour, generally in DESs and specifically in ethaline, distinctly differs from electron transfer in ILs and that the two solvent systems should be treated independently with respect to charge transfer. The ability to increase excited state stability, while providing tuneable solvent properties to control electron transfer reactions make ethaline a highly promising solvent for electron transfer applications.

Conflicts of interest

There are no conflicts to declare.

Data availability

The data supporting this article have been included as part of the supplementary information (SI). Supplementary data provides additional details on the following: synthesis of quenchers, viscosity modeling, photophysical characteriation data for $[Ru(bpy)_3]^{2+}$, electrochemical characterization $[Ru(bpy)_3]^{2+}$ and quenchers, and Stern-Volmer quenching data. See DOI: https://doi.org/10.1039/d5cp04727g. 2^+, electrochemical characterization $[Ru(bpy)_3]^{2+}$ and quenchers, and Stern-Volmer quenching data.

Notes and references

1 V. Hessel, N. N. Tran, M. R. Asrami, Q. D. Tran, N. Van Duc Long, M. Escribà-Gelonch, J. O. Tejada, S. Linke and K. Sundmacher, *Green Chem.*, 2022, **24**, 410–437.
2 J. J. Varghese and S. H. Mushrif, *React. Chem. Eng.*, 2019, **4**, 165–206.
3 D. R. Joshi and N. Adhikari, *J. Pharm. Res. Int.*, 2019, **28**, 1–18.
4 F. Pena-Pereira, A. Kloskowski and J. Namieśnik, *Green Chem.*, 2015, **17**, 3687–3705.
5 A. A. Quintana, A. M. Sztapka, V. d. C. Santos Ebinuma and C. Agatemor, *Angew. Chem. Int. Ed*, 2022, **61**, e202205609.
6 A. P. Abbott, D. Boothby, G. Capper, D. L. Davies and R. K. Rasheed, *J. Am. Chem. Soc.*, 2004, **126**, 9142–9147.
7 B. B. Hansen, S. Spittle, B. Chen, D. Poe, Y. Zhang, J. M. Klein, A. Horton, L. Adhikari, T. Zelovich, B. W. Doherty, B. Gurkan, E. J. Maginn, A. Ragauskas, M. Dadmun, T. A. Zawodzinski, G. A. Baker, M. E. Tuckerman, R. F. Savinell and J. R. Sangoro, *Chem. Rev.*, 2021, **121**, 1232–1285.
8 G. García, S. Aparicio, R. Ullah and M. Atilhan, *Energy Fuels*, 2015, **29**, 2616–2644.
9 Q. Zhang, K. De Oliveira Vigier, S. Royer and F. Jérôme, *Chem. Soc. Rev.*, 2012, **41**, 7108–7146.
10 R. Ratti, *Adv. Chem.*, 2014, **2014**, 1–16.
11 J. Płotka-Wasylka, M. de la Guardia, V. Andruch and M. Vilková, *Microchem. J.*, 2020, **159**, 1–12.
12 R. Germani, M. Orlandini, M. Tiecco and T. Del Giacco, *J. Mol. Liq.*, 2017, **240**, 233–239.
13 M. Natali, S. Campagna and F. Scandola, *Chem. Soc. Rev.*, 2014, **43**, 4005–4018.
14 S. Chatterjee, T. Chowdhury and S. Bagchi, *J. Phys. Chem. B*, 2024, **128**, 12669–12684.
15 N. Siraj, G. Grampp, S. Landgraf and K. Punyain, *Z. Phys. Chem.*, 2013, **227**, 105–119.
16 H. V. R. Annapureddy and C. J. Margulis, *J. Phys. Chem. B*, 2009, **113**, 12005–12012.
17 H. Y. Fu, Z. G. Xing, X. Y. Cao and G. Z. Wu, *Chin. Sci. Bull.*, 2013, **58**, 1882–1886.
18 A. Paul and A. Samanta, *J. Phys. Chem. B*, 2007, **111**, 1957–1962.
19 C. L. Bentley, A. M. Bond, A. F. Hollenkamp, P. J. Mahon and J. Zhang, *J. Phys. Chem. C*, 2014, **118**, 22439–22449.
20 C. L. Bentley, J. Li, A. M. Bond and J. Zhang, *J. Phys. Chem. C*, 2016, **120**, 16516–16525.
21 D. Behar, P. Neta and C. Schultheisz, *J. Phys. Chem. A*, 2002, **106**, 3139–3147.
22 R. C. Vieira and D. E. Falvey, *J. Phys. Chem. B*, 2007, **111**, 5023–5029.
23 A. Skrzypczak and P. Neta, *J. Phys. Chem. A*, 2003, 7800–7803.
24 G. Kodis, M. Z. Ertem, M. D. Newton and D. V. Matyushov, *J. Phys. Chem. Lett.*, 2022, **13**, 3297–3303.
25 H. Y. Lee, J. B. Issa, S. S. Isied, E. W. Castner, Y. Pan, C. L. Hussey, K. S. Lee and J. F. Wishart, *J. Phys. Chem. C*, 2012, **116**, 5197–5208.
26 M. Liang, A. Kaintz, G. A. Baker and M. Maroncelli, *J. Phys. Chem. B*, 2012, **116**, 1370–1384.
27 A. Pandey, A. Yadav and S. Pandey, *J. Lumin.*, 2017, **183**, 494–506.
28 D. Dhingra, A. Pandey and S. Pandey, *J. Phys. Chem. B*, 2019, **123**, 3103–3111, DOI: 10.1021/acs.jpcb.9b01193.
29 D. Dhingra, Bhawna, A. Pandey and S. Pandey, *J. Phys. Chem. B*, 2020, **124**, 4164–4173.
30 D. Dhingra, Bhawna, A. Pandey and S. Pandey, *J. Phys. Chem. B*, 2020, **124**, 4164–4173.
31 F. Zhen and P. Hapiot, *ChemElectroChem*, 2022, **9**, 1–6.
32 D. Shen, M. B. Vukmirovic and R. Akolkar, *J. Electrochem. Soc.*, 2019, **166**, E526–E532.
33 S. Fryars, E. Limanton, F. Gauffre, L. Paquin, C. Lagrost and P. Hapiot, *J. Electroanal. Chem.*, 2018, **819**, 214–219.
34 P. Qian, G. Cao, M. Muñoz, J. Vura-Weis, B. E. Gurkan, Z. Peng and J. Rodríguez-López, *Anal. Chem.*, 2025, **97**, 16239–16249.
35 C. A. Nkuku and R. J. LeSuer, *J. Phys. Chem. B*, 2007, **111**, 13271–13277.
36 A. Renjith and V. Lakshminarayanan, *J. Phys. Chem. C*, 2018, **122**, 25411–25421.
37 F. Zhen, L. Percevault, L. Paquin, E. Limanton, C. Lagrost and P. Hapiot, *J. Phys. Chem. B*, 2020, **124**, 1025–1032.
38 S. Spittle, I. Alfurayj, B. B. Hansen, K. Glynn, W. Brackett, R. Pandian, C. Burda and J. Sangoro, *JACS Au*, 2023, **3**, 3024–3030.
39 H. Li, Y. Chang, W. Zhu, C. Wang, C. Wang, S. Yin, M. Zhang and H. Li, *Phys. Chem. Chem. Phys.*, 2015, **17**, 28729–28742.

40 P. J. Smith and J. C. Goeltz, *J. Phys. Chem. B*, 2017, **121**, 10974–10978.

41 A. V. Dolganov, L. A. Klimaeva, E. E. Muryumin, S. G. Kostryukov, A. S. Kozlov, O. V. Tarasova and A. V. Knyazev, *Russ. J. Phys. Chem. A*, 2023, **97**, 2307–2313.

42 C. Campa, J. Camps, J. Font and P. De March, *J. Org. Chem.*, 1987, **52**, 521–525.

43 A. R. Harifi-Mood and R. Buchner, *J. Mol. Liq.*, 2017, **225**, 689–695.

44 B. G. Stevenson, E. H. Spielvogel, E. A. Loiaconi, V. M. Wambua, R. V. Nakhamiyayev and J. R. Swierk, *J. Am. Chem. Soc.*, 2021, **143**, 8878–8885.

45 R. Haghbakhsh, A. R. C. Duarte and S. Raeissi, *Molecules*, 2021, **26**, 1–19.

46 D. Lapeña, L. Lomba, M. Artal, C. Lafuente and B. Giner, *Fluid Phase Equilib.*, 2019, **492**, 1–9.

47 L. He, S. Su, Y. Zhao and J. Long, *J. Mol. Model.*, 2023, **29**, 101.

48 A. Vyšniauskas, I. López-Duarte, N. Duchemin, T. T. Vu, Y. Wu, E. M. Budynina, Y. A. Volkova, E. Peña Cabrera, D. E. Ramírez-Ornelas and M. K. Kuimova, *Phys. Chem. Chem. Phys.*, 2017, **19**, 25252–25259.

49 J. Hu and C. Y. Zhang, *Anal. Chem.*, 2013, **85**, 2000–2004.

50 A. M. Brouwer, *Pure Appl. Chem.*, 2011, **83**, 2213–2228.

51 J. Van Houten and R. J. Watts, *J. Am. Chem. Soc.*, 1976, **98**, 4853–4858.

52 K. Suzuki, A. Kobayashi, S. Kaneko, K. Takehira, T. Yoshihara, H. Ishida, Y. Shiina, S. Oishi and S. Tobita, *Phys. Chem. Chem. Phys.*, 2009, **11**, 9850–9860.

53 M. Borgwardt, M. Wilke, I. Y. Kiyan and E. F. Aziz, *Phys. Chem. Chem. Phys.*, 2016, **18**, 28893–28900.

54 A. Islam, N. Ikeda, A. Yoshimura and T. Ohno, *Inorg. Chem.*, 1998, **37**, 3093–3098.

55 J. P. Sauvage, J. P. Collin, J. C. Chambron, S. Guillerez, C. Coudret, V. Balzani, F. Barigelletti, L. De Cola and L. Flamigni, *Chem. Rev.*, 1994, **94**, 993–1019.

56 K. R. Barqawi, Z. Murtaza, T. J. Meyer, C. Hill and N. Carolina, *J. Phys. Chem.*, 1991, 47–50.

57 K. Hanson, M. K. Brennaman, A. Ito, H. Luo, W. Song, K. A. Parker, R. Ghosh, M. R. Norris, C. R. K. Glasson, J. J. Concepcion, R. Lopez and T. J. Meyer, *J. Phys. Chem. C*, 2012, **116**, 14837–14847.

58 J. V. Caspar and T. J. Meyer, *J. Phys. Chem.*, 1983, **87**, 952–957.

59 Q. Sun, S. Mosquera-vazquez, H. A. Goodwin, E. Vauthey and A. Hauser, *J. Am. Chem. Soc.*, 2013, **135**, 13660–13663.

60 Q. Sun, B. Dereka, E. Vauthey, M. L. Daku and A. Hauser, *Chem. Sci.*, 2017, 223–230.

61 I. M. Dixon, J.-L. Heully, F. Alary and P. I. P. Elliott, *Phys. Chem. Chem. Phys.*, 2017, **19**, 27765–27778.

62 D. Hernández-Castillo, R. E. P. Nau, M. A. Schmid, S. Tschierlei, S. Rau and L. González, *Angew. Chem., Int. Ed.*, 2023, **62**, 1–7.

63 J. Van Houten and R. J. Watts, *J. Am. Chem. Soc.*, 1976, **98**, 4853–4858.

64 A. Pandey, Bhawna, D. Dhingra and S. Pandey, *J. Phys. Chem. B*, 2017, **121**, 4202–4212.

65 A. M. Wright, A. A. Howard, J. C. Howard, G. S. Tschumper and N. I. Hammer, *J. Phys. Chem. A*, 2013, **117**, 5435–5446.

66 N. S. Hush, Intervalence-Transfer Absorption, Part 2. Theoretical Considerations and Spectroscopic Data, in *Progress in Inorganic Chemistry*, ed. F. A. Cotton, DOI: 10.1002/9780470166093.ch7.

67 P. Vath and M. B. Zimmt, *J. Phys. Chem. A*, 2000, **104**, 2626–2633.

68 O. A. Stasyuk, A. J. Stasyuk, M. Solà and A. A. Voityuk, *J. Nanostructure Chem.*, 2024, **14**, 293–306.

69 J. Bossert and C. Daniel, *Coord. Chem. Rev.*, 2008, **252**, 2493–2503.

70 S. Chattopadhyay, M. Mukherjee, B. Kandemir, S. E. J. Bowman, K. L. Bren and A. Dey, *Chem. Sci.*, 2021, **12**, 11894–11913.

71 S. Jakobsen, K. V. Mikkelsen and S. U. Pedersen, *J. Phys. Chem.*, 1996, **100**, 7411–7417.

72 E. M. Kober, J. V. Caspar, R. S. Lumpkin and T. J. Meyer, *J. Phys. Chem.*, 1986, 3722–3734.

73 R. J. Forster and T. E. Keyes, *J. Phys. Chem. B*, 1998, **102**, 10004–10012.

74 H. S. Geethanjali, D. Nagaraja and R. M. Melavanki, *J. Mol. Liq.*, 2015, **209**, 669–675.

75 M. Álvaro, E. Carbonell, B. Ferrer, H. Garcia and J. R. Herance, *Photochem. Photobiol.*, 2006, **82**, 185.

76 R. Lomoth, T. Häupl, O. Johansson and L. Hammarström, *Chem. – Eur. J.*, 2002, **8**, 102–110.

77 B. Wu, M. Liang, M. Maroncelli and E. W. Castner, *J. Phys. Chem. B*, 2015, **119**, 14790–14799.

78 B. Wu, M. Liang, N. Zmich, J. Hatcher, S. I. Lall-Ramnarine, J. F. Wishart, M. Maroncelli and E. W. Castner, *J. Phys. Chem. B*, 2018, **122**, 2379–2388.

79 C. M. Gordon and A. J. McLean, *Chem. Commun.*, 2000, 1395–1396.

80 M. Z. Hoffman, F. Bolletta, L. Moggi and G. L. Hug, *J. Phys. Chem. Ref. Data*, 1989, **18**, 219–543.

81 A. Pandey, R. Rai, M. Pal and S. Pandey, *Phys. Chem. Chem. Phys.*, 2014, **16**, 1559–1568.

82 S. Barani Pour, J. Jahanbin Sardroodi, A. Rastkar Ebrahimzadeh, G. Pazuki and V. Hadigheh Rezvan, *Sci. Rep.*, 2024, **14**, 1–18.

83 M. Chakraborty, T. Ahmed, R. S. Dhale, D. Majhi and M. Sarkar, *J. Phys. Chem. B*, 2018, **122**, 12114–12130.

84 D. Y. Chu and J. K. Thomas, *Macromolecules*, 1990, **23**, 2217–2222.

85 Y. Bai, P. Sun, M. Zhang, Z. Gao, Z. Yang and Y. Shao, *Electrochim. Acta*, 2003, **48**, 3447–3453.

86 T. Hamada, S. Tanaka, H. Koga, Y. Sakai and S. Sakaki, *Dalton Trans.*, 2003, 692–698.

87 J. R. Darwent and K. Kalyanasundaram, *J. Chem. Soc., Faraday Trans. 2*, 1981, **77**, 373–382.

88 C. M. Gordon and A. J. McLean, *Chem. Commun.*, 2000, 1395–1396.

89 A. J. McLean, M. J. Muldoon, C. M. Gordon and I. R. Dunkin, *Chem. Commun.*, 2002, 1880–1881.

90 M. Álvaro, E. Carbonell, B. Ferrer, H. Garcia and J. R. Herance, *Photochem. Photobiol.*, 2006, **82**, 185–190.

91 S. Farid, J. P. Dinnocenzo, P. B. Merkel, R. H. Young, D. Shukla and G. Guirado, *J. Am. Chem. Soc.*, 2011, **133**, 11580–11587.

92 T. P. Silverstein, *J. Chem. Educ.*, 2012, **89**, 1159–1167.

93 W. W. Parson, *J. Phys. Chem. B*, 2021, **125**, 7940–7945.

94 P. K. Ghorai and D. V. Matyushov, *J. Chem. Phys.*, 2006, **124**, 1–18.

95 R. A. Marcus, *Pure Appl. Chem.*, 1997, **69**, 13–29.

96 C. D. Clark and M. Z. Hoffman, *J. Phys. Chem.*, 1996, **3654**, 14688–14693.